



## Structure-based design of ligands of the m<sup>6</sup>A-RNA reader YTHDC1

Yaorong Li<sup>a,b</sup>, Rajiv Kumar Bedi<sup>a</sup>, Francesco Nai<sup>a</sup>, Valentin von Roten<sup>a</sup>, Aymeric Dolbois<sup>a</sup>, František Zálešák<sup>a</sup>, Raed Nachawati<sup>a</sup>, Danzhi Huang<sup>a</sup>, Amedeo Caflisch<sup>a,\*</sup>

<sup>a</sup> Department of Biochemistry, University of Zurich, Winterthurerstrasse 190, CH-8057, Zurich, Switzerland

<sup>b</sup> Department of Chemistry, Umeå University, SE-901 87, Umeå, Sweden

### ARTICLE INFO

#### Keywords:

RNA epigenetics  
Epitranscriptomics  
YTHDC1 binders  
Fragment-based drug discovery (FBDD)  
X-ray crystallography  
Molecular docking  
Molecular dynamics

### ABSTRACT

We report new chemical entities for disrupting the interactions between N6-methyladenosine (m<sup>6</sup>A) mRNA and its reader YT521-B homology-domain-containing protein 1 (YTHDC1). High-throughput docking was used to screen commercially available databases of small molecules, and molecular dynamics simulations were employed to evaluate the binding stability of m<sup>6</sup>A nucleotide analogues. The poses of 25 fragment-like new binders were confirmed by X-ray crystallography. The structure-based merging of two weak fragments resulted in a ligand-efficient binder (compound **6**) which shows an equilibrium dissociation constant of 1.7 μM in isothermal titration calorimetry measurements and a ligand efficiency value of 0.66 kcal mol<sup>-1</sup> n<sub>HA</sub><sup>-1</sup>.

### 1. Introduction

Recent studies on post-transcriptional and co-transcriptional modifications at the RNA level have led to a new subject called RNA epigenetics [1] or epitranscriptomics [2]. The N6-methyladenosine (m<sup>6</sup>A) modification is the most abundant internal chemical modification in messenger RNA (mRNA), and it has been the subject of intense investigations. The m<sup>6</sup>A modification plays essential roles in modulating many biological functions, including brain development [3], chromatin accessibility [4], heat shock response [5], immune response to infection [6], viral replications [7], and tumorigenesis [8]. The m<sup>6</sup>A deposition is widely considered a reversible and dynamic process [9], although these features might require further validation [10]. In a normal functional state, m<sup>6</sup>A cellular level is kept in homeostasis by several regulatory proteins. The m<sup>6</sup>A methylation is catalyzed by the METTL3/METTL14 methyltransferase [11,12], and is erased by the demethylases FTO [13] and ALKBH5 [14]. The downstream effects of m<sup>6</sup>A modification are elicited by m<sup>6</sup>A binding proteins (readers). Five direct reader proteins have been discovered so far: YTHDC1 [15], YTHDC2 [16] and YTHDF1-3 [15,17]. YTHDC1 is found almost exclusively in the nucleolus, while the other readers are primarily present in the cytosol [18].

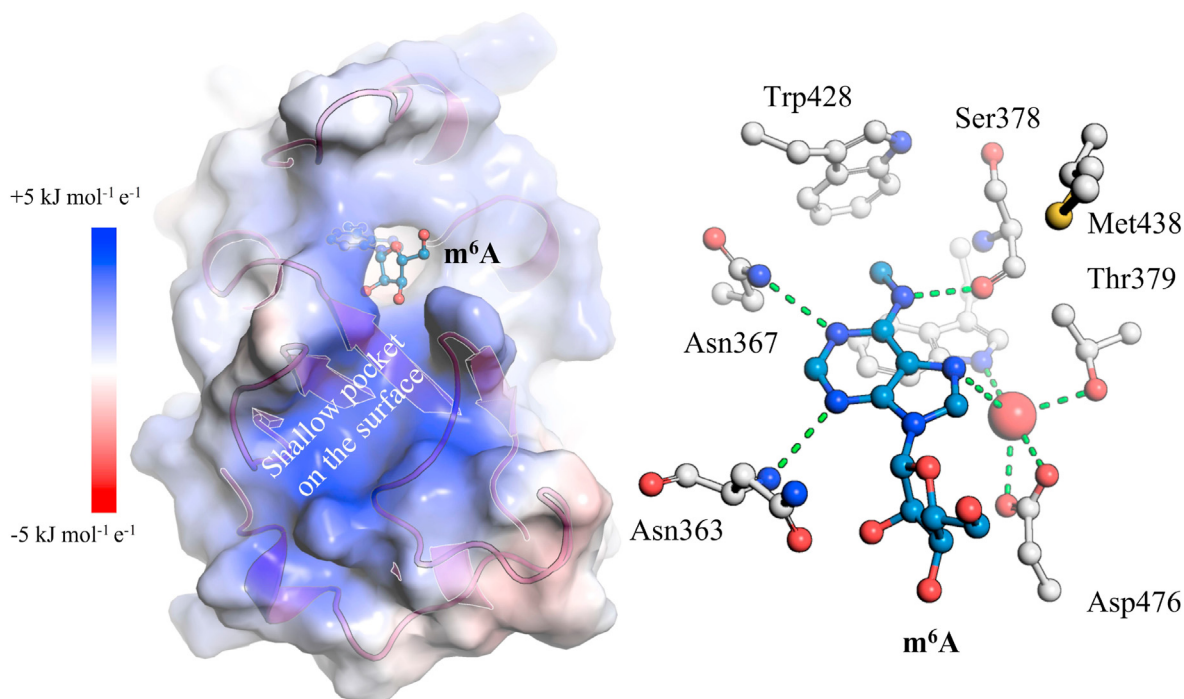
YTHDC1 regulates alternate splicing of m<sup>6</sup>A modified transcripts [19], mediates nuclear export of m<sup>6</sup>A-containing mRNA [20], and participates in XIST-mediated gene silencing [21]. More recently, two research groups independently found that YTHDC1 regulates the

functionalities of chromatin mediating the trimethylation at lysine 9 of histone H3 (H3K9me3) [22,23]. YTHDC1 is also involved in regulating the intracellular S-adenosyl-L-methionine (SAM) level by binding m<sup>6</sup>A-containing Methionine Adenosyltransferase 2A (MAT2A) mRNAs transcripts [24]. Concerning the role of YTHDC1 in disease, it was recently recognized as a potential pharmaceutical target for the treatment of acute myeloid leukemia (AML) [25] and possibly other types of cancer [26].

The YTH domain of YTHDC1 contains an aromatic cage evolved specifically for the binding of m<sup>6</sup>A [27]. Residues surrounding the cage (Fig. 1), protein dynamics, and structural water molecules play essential roles in the binding [28,29]. We have recently investigated the atomistic details of how the YTH domain of YTHDC1 recognizes m<sup>6</sup>A-containing RNA by combining molecular dynamics (MD) simulations and crystallography [28,30]. We also employed high-throughput docking to identify small-molecule binders. Protein X-ray crystallography and a biochemical assay were used to validate the docking results [31]. As these ligands were in the medium-high micromolar range of affinity, we decided to continue our efforts to search for more potent binders. In the present study, we first used high-throughput docking to screen for small-molecule ligands of the m<sup>6</sup>A-recognition domain of YTHDC1. By combining structural features of two small-molecule ligands, we have designed a low micromolar binder of YTHDC1 which we have validated by X-ray crystallography, a biochemical assay, and isothermal titration calorimetry (ITC).

\* Corresponding author.

E-mail address: [caflisch@bioc.uzh.ch](mailto:caflisch@bioc.uzh.ch) (A. Caflisch).



**Fig. 1.** Crystal structure of the complex of YTHDC1 with the  $m^6A$  nucleoside (PDB 6ZCN). (Left) The electrostatic potential at the RNA-recognition surface of YTHDC1 is mainly positive. The electrostatic potential was calculated using the APBS 2.1 plugin of PyMOL [32]. (Right) The detailed view of the binding mode shows the network of hydrogen bonds (green, dashed lines) between  $m^6A$  (carbon atoms in cyan) and YTHDC1 residues (carbon atoms in grey) or the conserved water molecule (red sphere). (For interpretation of the references to colour in this figure legend, the reader is referred to the Web version of this article.)

## 2. Results and discussion

This work reports 25 small-molecule binders of the  $m^6A$ -reader domain of YTHDC1. (In the following text, the term YTHDC1 is used frequently as an abbreviation for the  $m^6A$ -recognition domain of YTHDC1). The new ligands are divided into four groups according to their chemical structures and/or interactions with YTHDC1 (Table 1 and Fig. 2). Group 1 includes analogues of the  $m^6A$  nucleobase. They were expected to improve the binding affinity and ligand efficiency (which is the binding free energy divided by the number of heavy, i.e., non-hydrogen atoms,  $n_{HA}$ ) by exploring additional interactions with the binding site (Fig. 2a). Group 2 binders form two hydrogen bonds between their *N*-methyl amide moiety and two polar residues in the binding pocket (Fig. 2b). The third group of compounds are characterized by interactions between their morpholine (pyrrolidine in compound 24) and the aromatic cage (Fig. 2c). Most of these compounds displace the recognition loop, which results in a larger aperture of the binding site. Group 4 includes a compound that displaces the structural water molecule [28] (Fig. 2d) and other chemotypes (Fig. 2e).

### 2.1. Improving ligand efficiency by replacing the ribose of the $m^6A$ nucleoside

The  $m^6A$  nucleoside is recognized by the aromatic cage of YTHDC1 in which three residues, namely, Ser378, Asn367, and Asn363, form hydrogen bonds with the nucleobase (Fig. 1). The N6-methyl group further strengthens the ligand-protein binding by van der Waals (vdW) interactions with the lipophilic binding site. Although the ribose ring presents multiple hydrogen-bond interactions with its surrounding residues, these residues are solvent-exposed and thus may not significantly contribute to the binding affinity (Figure S1). We, therefore, first tested the binding affinity of the  $m^6A$  nucleobase by a homogenous time-resolved fluorescence-based (HTRF) assay [33]. The removal of the ribose group results in a twofold reduction in binding affinity with an improvement in ligand efficiency from 0.23 to 0.38 kcal mol<sup>-1</sup> n<sub>HA</sub><sup>-1</sup>

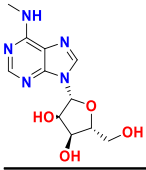
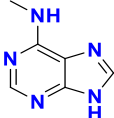
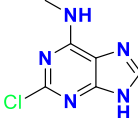
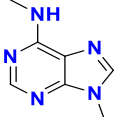
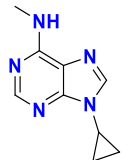
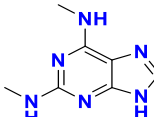
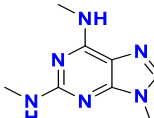
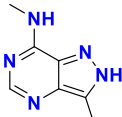
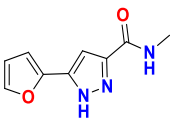
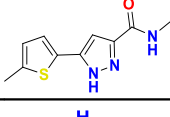

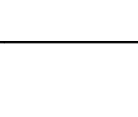
(Table 1). This result encouraged us to explore fragment analogues of the  $m^6A$  nucleobase. We searched the analogues via the small-molecule catalog Chemspace (<https://chem-space.com/>) and identified ten fragments. We then decided to run multiple MD simulations (of 5 ns each) to evaluate the stability of their predicted binding modes with YTHDC1. We finally decided to test *in vitro* the five fragments that showed stable binding modes in the MD simulations. One of the five derivatives of the  $m^6A$  nucleobase was purchased from a commercial vendor (compound 1), while the derivatives 2 to 5 were synthesized in-house. The HTRF assay shows that the fragments 1–3 have a nearly threefold affinity improvement and similar ligand efficiency as the  $m^6A$  nucleobase (Table 1). Furthermore, the crystal structures of the complex with the YTH domain of YTHDC1 show essentially the same binding mode as the nucleobase of the  $m^6A$  nucleoside (Figure S2a).

Near the  $m^6A$  binding site, a positively charged shallow pocket binds the negatively charged RNA (Fig. 1) [30]. Considering the beneficial effect that simple substitutions at N9 had on affinity (methyl in compound 2 and cyclopropyl in compound 3, Figure S1 and S2a), we propose to grow the fragments into the positively charged sub-pocket by linking the nucleobase with polar groups. Another possible position for substitution is C2 between N1 and N3 of the  $m^6A$  nucleobase (Fig. 2a). The chloride substituent (compound 1) in this position fits a small lipophilic pocket (PDB ID: 7P88). We also tried different substituents in this position, such as the methylamine group (compounds 4 and 5), but the results were not satisfactory. However, X-ray structures [31] and MD simulations (Figure S3) show that the side chain of Asn364 can adopt different conformations and thus provide extra space for further exploration.

### 2.2. Hydrogen bond to the side chain of Asp476

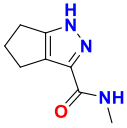
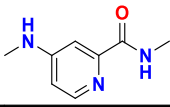
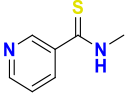
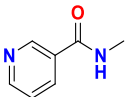

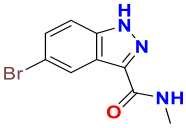
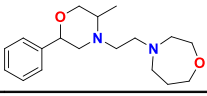
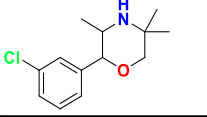
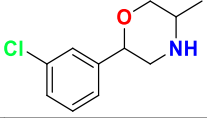
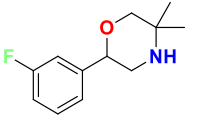
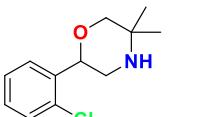
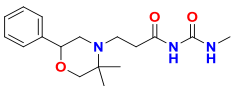
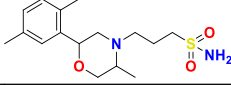
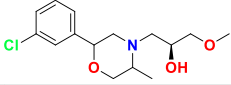
The compounds in group 2 feature a heteroaromatic ring substituted with *N*-methylamide except for compound 12 which has an *N*-methylthioamide (Table 1). The *N*-methylamide is involved in hydrogen-bond interactions with the backbone carbonyl group of Ser378 and the side chains of Asn367. Furthermore, their *N*-methyl groups fit favourably in

**Table 1**Chemical structure and binding affinity of 25 ligands of the YTHDC1 m<sup>6</sup>A-recognition domain.

Internal Name	2D structure	Residual signal <sup>a</sup>	IC <sub>50</sub> [μM] <sup>b</sup>	PDB code Resolution [Å]	LE <sup>c</sup>	In-silico Method <sup>d</sup>
Group 1 m <sup>6</sup> A nucleoside		32%	504 (56)	6ZCN (1.6)	0.23 (0.29)	–
m <sup>6</sup> A nucleobase		49%	918	–	0.38	–
1		35%	359	7P88 (1.5)	0.39	MD
2		23%	306	7P8A (1.7)	0.40	MD
3		19%	294	7P8B (1.2)	0.34	MD
4		72%	–	–	–	MD
5		Nd <sup>d</sup>	–	–	–	MD
6		3%	39 (1.68)	7P8F (1.5)	0.50 (0.66)	MD
Group 2 7		23%	384	7PJP (1.6)	0.33	Vina
8		Nd <sup>d</sup>	–	7PJ7 (1.4)	–	Vina
9		69%	–	7P87 (1.3)	–	MD
10		90%	–	6YKZ (1.2)	–	Vina

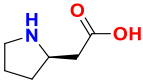
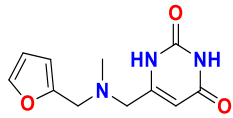
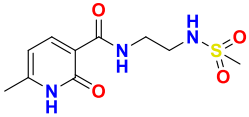
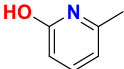
(continued on next page)

Table 1 (continued)

Internal Name	2D structure	Residual signal <sup>a</sup>	IC <sub>50</sub> [μM] <sup>b</sup>	PDB code Resolution [Å]	LE <sup>c</sup>	In-silico Method <sup>d</sup>
						
11		73%	–	6YKJ (1.6)	–	Vina
12		77%	–	7PJQ (1.2)	–	SEED
13		97%	–	6YNP (1.1)	–	SEED
14		64%	–	7PJ8 (1.4)	–	Vina
15		Nd <sup>d</sup>	–	7PJ9 (1.7)	–	Vina
Group 3						
16		84%	–	6YKI (1.3)	–	Vina
17		88%	–	6YNI (1.36)	–	Vina
18		84%	–	6YL8 (1.5)	–	Vina
19		89%	–	6YKE (1.52)	–	Vina
20		74%	–	6YNJ (1.5)	–	Vina
21		Nd <sup>d</sup>	–	6YNL (1.5)	–	Vina
22		89%	–	6YL9 (1.5)	–	Vina
23		91%	–	6YNM (1.5)	–	Vina

(continued on next page)

Table 1 (continued)

Internal Name	2D structure	Residual signal <sup>a</sup>	IC <sub>50</sub> [μM] <sup>b</sup>	PDB code Resolution [Å]	LE <sup>c</sup>	In-silico Method <sup>d</sup>
24		88%	–	7PJB (1.9)	–	SEED
Group 4						
25		85%	–	6YNK (1.3)	–	Vina
26		56%	–	6YOQ (1.3)	–	SEED
27		74%	–	7PJA (1.9)	–	SEED

<sup>a</sup> Residual HTRF signal in the presence of the small-molecule ligand at a concentration of 1 mM. The lower the residual signal (in percentage) the higher the affinity of the small-molecule ligand. There is no evidence of binding for compounds 4 and 5.

<sup>b</sup> IC<sub>50</sub> values derived from the HTRF competition assay are reported for the compounds whose residual activities at 1 mM compound concentration are smaller than 50%. The values in parentheses for the m<sup>6</sup>A nucleoside and compound 6 are the K<sub>d</sub> values measured by ITC.

<sup>c</sup> The ligand efficiency (LE) values are calculated according to the equation  $LE = -\frac{\Delta G}{n_{HA}} = -RT \frac{\ln K_d}{n_{HA}} \approx -RT \frac{\ln IC_{50}}{n_{HA}}$ , where ΔG is binding free energies from ITC (unit in kcal/mol), n<sub>HA</sub> number of heavy atoms, IC<sub>50</sub> from the HTRF assay, R molar gas constant, and T temperature in Kelvin (298 K in this calculation). Most LE values are calculated by substituting IC<sub>50</sub> for K<sub>d</sub> values. For the m<sup>6</sup>A nucleoside and compound 6 the LE values were calculated using both IC<sub>50</sub> value and K<sub>d</sub> and the latter is shown in parentheses.<sup>d</sup> Different in-silico methods were used for screening or optimizing the compounds, including MD simulations and automatic docking by AutoDock Vina [37] or SEED [38,39].

<sup>d</sup> Nd = Not determined because of interference or solubility issues.

the aromatic cage (Fig. 2b). The most active compound in this group (compound 7, PDB ID: 7PJP) shows comparable binding affinity and more favorable ligand efficiency than the m<sup>6</sup>A nucleoside (IC<sub>50</sub> = 384 μM, Figure S4). The two nitrogen atoms of the pyrazole ring of compound 7 form two hydrogen bonds with Asp476 and a structural water molecule [28] (Fig. 2b). Furthermore, its furan ring is involved in a cation-π interaction with the side chain of Arg404, while a similar interaction is not well-defined for the thiophene compound 8 (PDB ID: 7PJ7, Figure S2b). The favorable N-methylamide substituent is present in different heteroaromatic rings, but the pyrazole attachment shows the strongest binding affinity in this group. Previously, we reported an N-methylamide substituted indazole with similar potency (compound 26 of Ref. [31]) which shows similar interactions as the ligands in group 2.

### 2.3. Improving binding and ligand efficiency by merging hydrogen-bonding interactions

Compound 7 and m<sup>6</sup>A form four hydrogen bonds with the aromatic cage. Three of these hydrogen bonds are in common, i.e., with residues Ser378, Asn367, and the conserved water molecule (Fig. 2). In addition, compound 7 acts as a hydrogen bond donor to the side chain of Asp476. Inspired by the crystal structures, we designed compound 6, which was predicted to form the four hydrogen bonds mentioned above (Fig. 3). We then used ChemAxon [34] to predict the dominant tautomers at pH = 7.4. The tautomeric state in which the pyrazole ring can form two hydrogen bonds with the reader protein has a population of 96% compared to the 3% for the tautomer with the H atom on the other nitrogen atom.

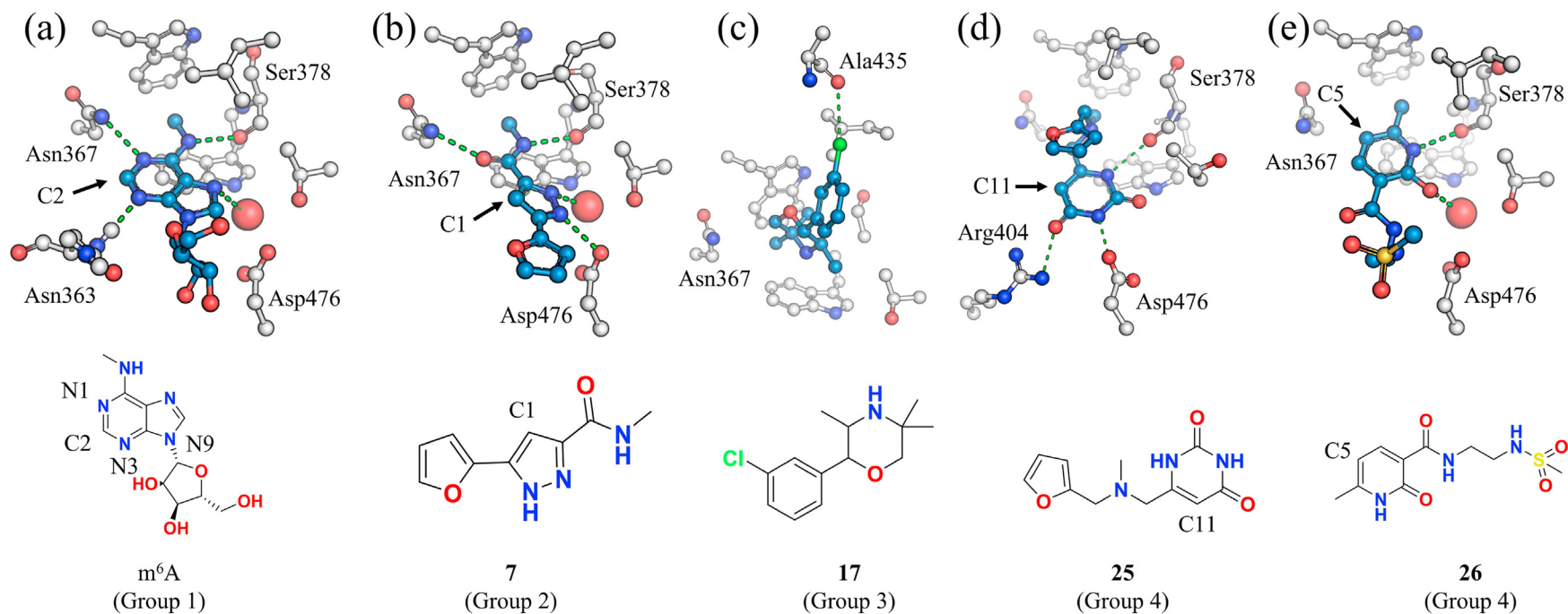
We then ran multiple MD simulations (five runs of 20 ns each for each tautomer) to check the stability of the proposed binding poses. For both tautomers, the starting structures were based on the X-ray structure of the m<sup>6</sup>A nucleoside (PDB ID: 6ZCN) [31]. During the simulations, the highly populated tautomer showed a stable binding pose with its RMSD values mostly around 1 Å (Figure S5). In contrast, the less populated tautomer deviated from the reference structure more than 3 Å and fully dissociated from the binding pocket in three of the five MD runs. The predicted

stability of the bound state of the most populated tautomer encouraged us to purchase this compound (from Chempspace). The HTRF assay showed an IC<sub>50</sub> value of 39 μM for compound 6, and ITC further confirmed its binding (with an equilibrium dissociation constant K<sub>d</sub> = 1.7 μM, Figure S6). Protein X-ray crystallography finally validated the predicted binding pose (Fig. 3). Compared to the m<sup>6</sup>A nucleoside, compound 6 shows an approximately 15-fold lower IC<sub>50</sub> value and 30-fold improvement in the equilibrium dissociation constant measured by ITC (1.7 kcal mol<sup>-1</sup> vs. 56 kcal mol<sup>-1</sup>). The binding affinity of compound 6 is even comparable to that of the RNA sequence motif GG(m<sup>6</sup>A)CU (K<sub>d</sub> = 0.5 μM) [30]. Importantly, the ligand efficiency improved from 0.29 (m<sup>6</sup>A nucleoside) to 0.66 kcal mol<sup>-1</sup> n<sub>HA</sub><sup>-1</sup> based on the ITC data, and thus compound 6 is a good starting point for further development. Moreover, compound 6 shows weak binding to YTHDF3 at a concentration of 1 mM (Table S1).

### 2.4. Enlarging the binding pocket by morpholine compounds

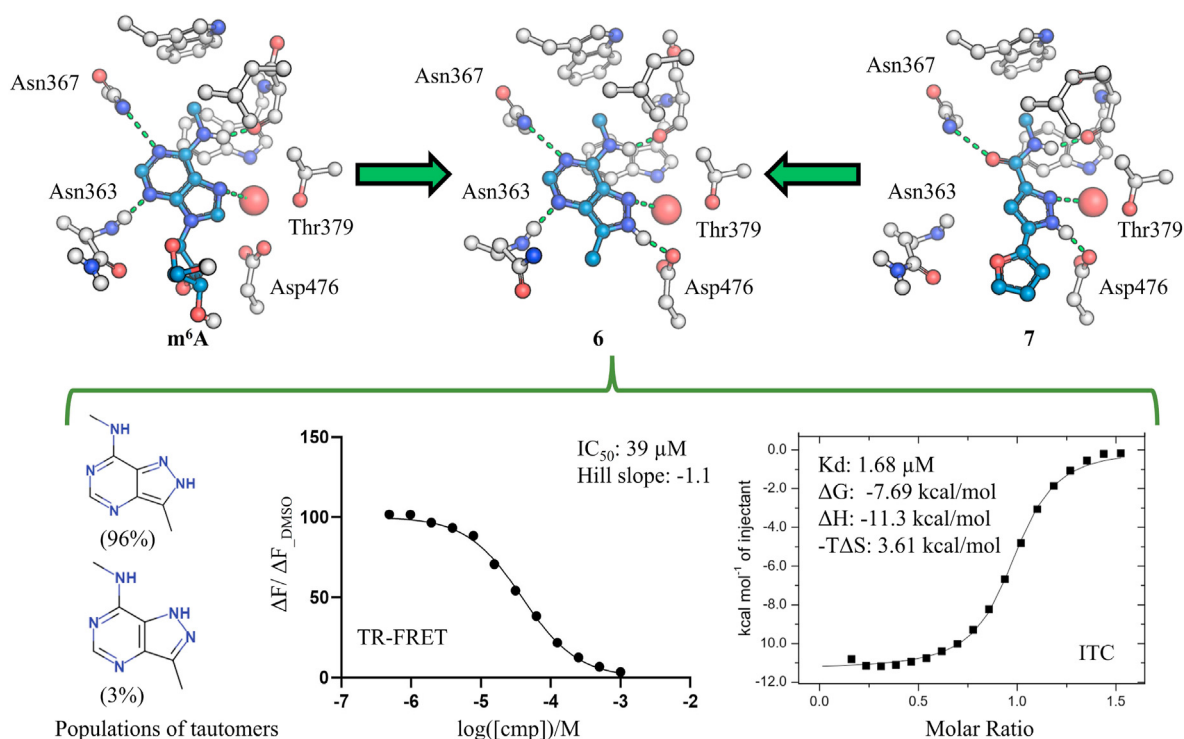
The morpholine series shows a displacement of the recognition loop by about 2–5 Å for the Cα atom at the tip of the loop, i.e., residue Gly433 (Fig. 2c and Group 3 in Table 1). The loop opening enlarges the binding site's volume, thereby permitting more space for further exploration, which is illustrated in the structural overlap of the structures 6ZCN and 6YNI (Figure S7). We then used MarvinSketch to calculate the population of the protomers [34]. In solution, the morpholine is positively charged with a probability ranging from 5% for compound 16–90% for compound 17. In the charged state, the morpholine ring forms a cation-π interaction with the aromatic cage, and its methyl or dimethyl substituents are deeply buried in the binding cage. The benzene ring extending from the morpholine is responsible for the displacement of the recognition loop, and different substituents are permitted on the benzene, for example, methyl, chloride, and fluorine groups (Table 1). The meta-chloride substituent on the phenyl (compound 17) forms a halogen bond with the backbone carbonyl of Ala435 (Fig. 2c).

A sulfate ion from the crystallization solution was observed near the charged morpholine in the binding pocket. Therefore, we tried to link it



**Fig. 2.** Representatives of the four groups of ligands (PDB codes 6ZCN, 7PJP, 6YNI, 6YNK, and 6YOQ from left to right). **(Top row)** The binding modes from the crystal structures show the hydrogen bonds (green, dashed lines) between residues in the  $m^6A$ -recognition pocket (carbon atoms in grey) and the ligands (carbon atoms in cyan). The conserved water molecule is indicated by a red sphere. The water molecule is not shown in panels c and d as it is not present in the complexes with compounds 17 and 25, respectively. These pictures were prepared using the software PyMOL [32]. **(Bottom row)** Chemical structures. Table 1 contains the chemical structures of all ligands and their binding affinity for the YTH domain of YTHDC1. (For interpretation of the references to colour in this figure legend, the reader is referred to the Web version of this article.)





**Fig. 3.** Structure-guided merging of ligands. The ITC thermogram and HTRF dose-response curve are shown for compound **6** and the YTH domain of YTHDC1. The populations of the two tautomers of compound **6** in an aqueous solution were predicted by ChemAxon [34].

to the morpholine by attaching an ethanesulfonamide group (compound **22**). The linked compound roughly maintains the original pose but seems to suffer high ligand strain energy in the sub-pocket (PDB ID: 6YL9). The strain explains, at least in part, why compound **22** does not show an improved binding. Optimizing the linker length could be an option for releasing the high strain energy. Flexible substituents on the N atom of the morpholine ring were designed to reach the Asp476 side chain but did not show any affinity improvement, e.g., compounds **16**, **21**, and **23**. The flexible substituents of these compounds cannot be modeled in the electron density, indicating that less effective interactions exist between them and the solvent-exposed region of the binding site.

### 2.5. Replacing the structural water molecule by uracil compounds

Our previous study showed that replacing the conserved water molecule (that acts as bridges for hydrogen bonds with the side chains of Trp377 and Asp476) with uracil-containing ligands results in approximately 2 kcal mol<sup>-1</sup> penalty in binding free energy [28]. Nonetheless, the uracil derivatives (e.g., compound **25**) show promising interactions with YTHDC1. First, the uracil moiety forms five hydrogen bonds with surrounding residues, providing binding specificity (Fig. 2d). Second, substitution is possible for its free carbon atom position, thereby permitting the exploration of the sub-pocket which C11 of compound **25** points to.

If compound **25** is protonated on the tertiary amino group, its positive charge can form a cation- $\pi$  interaction with the aromatic cage (Figure S8). In addition, the amino group could act as a donor for a hydrogen bond with the carbonyl oxygen of Ser378. However, we cannot examine this possibility solely based on the crystal structure. We thus resorted to in-silico methods. The population of the protonated state was predicted as 38% in aqueous solution compared to 62% for the neutral form, and the strain energy of the ligand in the bound pose is small for both forms (by OpenEye's Freeform) [35,36]. Multiple MD simulations show substantially higher structural stability for the neutral state than the charged species by comparing their pose RMSD values, approximately 1 Å vs. 5 Å, respectively (Figure S8). This simulation result is consistent with the charge state of the natural ligand, as m<sup>6</sup>A does not

bear any formal charge. Therefore, further optimization on this series shall aim to stabilize the neutral protomer rather than focusing on a positively charged (tertiary) amino group.

Compound **26** shows moderate binding affinity (56% residual signal at 1 mM) with YTHDC1 and offers a possibility for further optimization. This compound captures most of the interactions which m<sup>6</sup>A does with YTHDC1 (Fig. 2e). For example, the 2-pyridone core forms hydrogen bonds with Ser378 and the structural water molecule. The aromatic cage recognizes the 6-methyl group. By analyzing its crystal structure (PDB ID: 6YOQ), we find that replacing C5 of the 2-pyridone ring with a nitrogen atom may introduce an extra hydrogen bond to Asn367. Moreover, the solvent-exposed sulfonamide group does not show specific interactions with the reader domain. Therefore, it could be used as a linker for growing fragments to the solvent-exposed pocket.

## 3. Conclusion

In summary, we have identified 25 small-molecule ligands of the YTH domain of YTHDC1 by in silico methods, i.e., molecular docking and molecular dynamics simulations. Their crystal structures in the complex with YTHDC1 were solved at high resolution (1.2–1.9 Å). The SAR of the ligands and their interactions with YTHDC1 were used to suggest directions for hit optimization. The merging of two weak ligands, namely the m<sup>6</sup>A nucleobase (IC<sub>50</sub> = 900 μM) and compound **7** (IC<sub>50</sub> = 400 μM), has resulted in the ligand-efficient compound **6** (IC<sub>50</sub> = 39 μM) which has K<sub>d</sub> = 1.7 μM as measured by ITC and a ligand efficiency of 0.66 kcal mol<sup>-1</sup> n<sub>HA</sub><sup>-1</sup>. Furthermore, compound **6** does not show significant binding to the off-target YTHDF3.

## 4. Materials and methods

### 4.1. Docking-based virtual screening (VS)

Two docking engines were used to screen small-molecule libraries in this study, namely, Autodock Vina 1.1.2 [37] and SEED [38,39]. In this virtual screening campaign, our focus was to efficiently search for

potential hit compounds for further experimental validation. Protein flexibility was not taken into account despite its potential usefulness [40].

The structure of YTHDC1 in complex with the oligoribonucleotide GG(m<sup>6</sup>A)CU (PDB ID: 4R3I) [27] was used for the docking campaign. The structure was prepared for docking using the same procedure as for the MD simulations (see below). After the minimization, the oligoribonucleotide, all the water molecules, and ions were removed from the system. In the VS stage by docking, we decided to remove all solvent molecules to allow for a large variety of putative binding modes. Interestingly, the docking programs suggested also ligands that replace the conserved water molecule (Fig. 2d). The continuum electrostatics treatment of the solvent (see below) approximates the water molecules, including the conserved ones, by a high-dielectric region which results in a favorable contribution for polar groups of the ligand. On the other hand, the presence of water molecules would not allow for the placements of ligand atoms because of van der Waals repulsion.

For the screening with AutoDock Vina, the binding site was defined by a 30 × 30 × 30 Å cubic grid box centered on the geometric center of the m<sup>6</sup>A nucleoside coordinates. We set the parameter “exhaustiveness” to 10 to explore the configurational space of ligands and left the rest of the parameters as the default. Only the best-scoring poses were saved for further analysis. About 0.4 million molecules from the ZINC's fragment sub-chemical database [41] were screened. After docking with Vina, we only considered the top 1000 molecules ranked by the predicted ligand efficiency, i.e., docking score divided by the number of heavy atoms. The final potential hit list was pruned by discarding compounds with less than three hydrogen bonds with YTHDC1.

The docking program SEED with its polar docking mode was used to screen small ( $n_{\text{HA}} < 20$ ) and mainly rigid molecules (about 0.1 million from ZINC). The fragments were placed by SEED with at least one hydrogen bond to the backbone polar groups or side chain of residue Ser378 which was considered as the center of the binding site. The residues within 15 Å of Ser378 were taken into account for the calculations of electrostatic and van der Waals energy terms. The specifications of ligand atoms for the binding site definition are optional in SEED, and in this case, it was not necessary because Ser378 is deeply buried in the m<sup>6</sup>A binding site. SEED uses an efficient procedure for the numerical calculation of the Born radii [42,43] which are used for the evaluation of the generalized Born electrostatic energy terms. The docking with SEED approximately required 1–5 s for each molecule, while the docking with AutoDock Vina required about 20 s.

#### 4.2. Pose validation by MD simulations

All systems were prepared based on the m<sup>6</sup>A-YTHDC1 complex X-ray structure (PDB ID: 6ZCN) [28]. Chain A of the structure was used as the template to construct other complex systems. The protein (residue 345 to 506), ligand (i.e., m<sup>6</sup>A nucleoside), and crystal water molecules were mainly kept while the other buffer components were removed. Protonation states of all ionizable residues were determined based on their pK<sub>a</sub> values in water and interaction environments with the protein. Missing atomic coordinates were built using the IC tables of CHARMM36 force field parameters [44,45]. Each system was solvated with a 70 Å rhombic dodecahedron (RHDO) water box to ensure a 12 Å buffer water layer between the protein system and the boundary of the water box. To neutralize and mimic physiological conditions, we set the ionic concentration of the system to 150 mM with Na<sup>+</sup> and Cl<sup>-</sup> ions. MD simulations were used to check the structural stability of the predicted pose of 15 compounds. Ten m<sup>6</sup>A analogues were designed based on the crystal pose of m<sup>6</sup>A, and five of them showing stable poses during MD simulations, namely compounds 1–5, were purchased or synthesized. Another five compounds with *N*-methylamide pyrazole were designed based on the ligand pose in the X-ray structure 6T0C [31], and only compound 9 was purchased. The ligand modifications were performed in Maestro-2018 [46].

Each system was initially energy minimized for 10 000 steps with a

series of constraints and restraints to eliminate bad contacts and poor geometry between atoms. The minimized structure was heated to 300 K and equilibrated in NVT condition (constant volume and temperature). During the equilibration, the heavy atoms of the protein and ligand were restrained to the minimized model with harmonic potentials. The restraints applied to the complex were slowly released, followed by additional equilibration without restraints. The equilibration at NVT lasted for 500 ps. The temperature was controlled by the Nosé–Hoover thermostat [47]. The system was then switched to NPT condition (constant pressure and temperature) for a pre-production MD simulation, and it lasted for 200 ps. The pressure was kept at 1 atm and controlled by the Langevin piston algorithms [48]. After the entire equilibration phase, a 5 ns of production MD simulation was performed on most systems. For compounds 6 and 25, we carried out MD simulations for their different tautomers and protonation states bound to YTHDC1. Five replicas were carried out for each state with different starting velocities, and each replica was sampled for 20 ns.

The protein was represented by the CHARMM36 force fields [45], water molecules by the TIP3P model, and ligands by CGenFF [49]. The SHAKE algorithm was applied to all bonds involving hydrogen atoms. The particle mesh Ewald summation (PME) method [50] was used for electrostatic interactions with a 12 Å real-space cutoff. The switching function was applied between 10 Å and 12 Å for the van der Waals interactions. During each MD simulation, atomic coordinates were saved at one ps time intervals for later analysis. All simulations and analyses were carried out using the CHARMM program (version c42b2) [51].

#### 4.3. Protein expression, purification, and X-ray crystallography

Recombinant YTH domain of YTHDC1 protein comprising residues 345–509 (YTHDC1 345–509) was expressed in *E. coli* and purified as described in detail previously [30]. In summary, the N-terminally hexahistidine-tagged YTH domain was purified using immobilized metal affinity chromatography (IMAC) followed by size exclusion chromatography. Crystal structures of the YTH domain in complex with the compounds were obtained by soaking compounds into the crystals of YTHDC1 as reported before [31].

#### 4.4. Binding assays

The residual signals at 1 mM compound concentration and the IC<sub>50</sub> values were obtained through an HTRF-based assay as previously described [31,33]. The assay evaluates the binding interaction of the YTHDC1 YTH domain (amino acids 345–509) and a methylated RNA (sequence: 5'-Biotin-AAGAACCGG(m<sup>6</sup>A)CUAAGCU-3'). The YTH domain of YTHDC1 is expressed as a GST-fusion protein that is recognized by an anti-GST antibody labelled with Eu<sup>3+</sup>, acting as the Förster resonance energy transfer (FRET) donor. The biotinylated RNA is bound by Streptavidin conjugated to XL665, the FRET acceptor. The binding of the methylated RNA to the YTH binding site leads to the formation of a four-member complex constituted by the GST-tagged YTH domain of YTHDC1, anti-GST Eu<sup>3+</sup>-labelled antibody, biotinylated RNA, and Streptavidin conjugated to XL665. This complex formation subsequently leads to the proximity between the FRET donor and acceptor, resulting in a signal emission. Suppose the tested compound can compete with the methylated RNA for the occupation of the YTH active site, the emitted signal decreases. The assay mix includes 25 nM YTHDC1 YTH domain-GST fusion protein, 15 nM biotinylated RNA (Dharmacon), 0.8 nM anti-GST Eu<sup>3+</sup>-conjugated antibody (Cisbio, 61GSTKLB), 1.875 nM XL665-conjugated streptavidin (Cisbio, 610SAXLB), and the compound of interest. The compound concentration in the final mix strictly depends on the assay's aims. It is fixed at 1 mM to investigate the residual signal or set as an array of 1 mM 2-fold dilutions to determine the IC<sub>50</sub> values. The assay's components are diluted in a buffer composed of 50 mM HEPES pH 7.5, 150 mM NaCl, 100 mM K<sub>2</sub>SO<sub>4</sub>, and 0.1% BSA. The reagents mix is incubated for 3 h at 24 °C, transferred into a white, low volume 384-well



plate (Corning, 4513), and measured using an Infinite M1000 plate reader (Tecan).  $\text{Eu}^{3+}$  is excited at a wavelength of 317 nm, and fluorescence emissions are measured at 620 and 665 nm, with an excitation/emission lag time of 60  $\mu\text{s}$ . The  $\text{IC}_{50}$  values were obtained by analyzing the dose-response data.

The isothermal titration calorimetry (ITC) experiment was carried out at 18 °C using MicroCal ITC200 (GE Healthcare). The final gel filtration of the protein was performed in 20 mM Tris pH 7.4 and 150 mM NaCl. The protein sample at the concentration of 1.1 mM was titrated into the sample cell containing 150  $\mu\text{M}$  compound dissolved in gel filtration buffer. After an initial injection of 0.4  $\mu\text{L}$ , 19 injections of 2.0  $\mu\text{L}$  each were performed. The raw data were integrated and analyzed using a single-binding-site model provided in the MicroCal Origin software package.

#### 4.5. Chemistry

All reagents were used as received unless otherwise noted. The solvents were dried over activated molecular sieves of appropriate size. All reactions were monitored by TLC or NMR. Chromatography was carried out over silica gel by hand or automated flash chromatography (Büchi C-850 flash prep).  $^1\text{H}$  and  $^{13}\text{C}$  NMR spectra were recorded on AV2 400 MHz Bruker spectrometer. Chemical shifts are given in ppm. The spectra are calibrated to the residual  $^1\text{H}$  and  $^{13}\text{C}$  signals of the solvents. Multiplicities are abbreviated as follows: singlet (s), triplet-triplet (tt), multiplet (m), and broad (br). Melting points were determined on a Büchi M-560 melting point instrument. High-resolution electrospray ionization mass spectrometry was performed on an Agilent 1290 Infinity LC system coupled to an Agilent 6540 quadrupole time-of-flight mass spectrometer. The jet stream electrospray source was operated in positive mode with the following parameter settings: nebulizer pressure 35 psig, nozzle voltage 0 V, sheath gas flow 11 L/min, sheath gas temperature 375 °C, drying gas flow 8 L/min, drying gas temperature 250 °C, capillary voltage 3000 V and fragmentor voltage of 175 V. Accurate mass spectra were acquired in profile mode over an  $m/z$  range of 100–1000 by 1 spectrum per second. The Q-TOF instrument was operated in high-resolution mode with 1700  $m/z$  instrument mass range at a resolving power of 33 000 (measured at  $m/z$  322). The purity was acquired by HPLC on an Agilent LC device using a NUCLEOSHELL RP18 column (50  $\times$  4.6 mm, 2.7  $\mu\text{m}$ ). The eluent at flow rate of 1.5 mL/min consisted of MeCN and 0.01 M  $(\text{NH}_4)_2\text{HPO}_4$  pH = 6.6 as solvents. All compounds showed  $\geq 95\%$  purity. MarvinSketch [34] was used for drawing, displaying, and characterizing chemical structures and protonation states as well as for generating conformers.

##### 4.5.1. *N*,9-Dimethyl-9H-purin-6-amine (compound 2)

To a stirred suspension of 6-chloro-9-methyl-9H-purine (100 mg, 0.59 mmol) in isopropanol (2 mL), methylamine (3 equiv., 1.78 mmol, 222  $\mu\text{L}$ , 8 M in EtOH) was added. The reaction mixture was stirred at 80 °C for 2 h in the microwave and concentrated under reduced pressure. The crude residue was purified by column chromatography (EtOAc/heptane = 9:1 to EtOAc/MeOH = 100:5 to 100:20) to afford the desired product as a yellow solid (85 mg, 88% yield). HPLC Purity = 100%; Mp: 187–188 °C;  $^1\text{H}$  NMR (400 MHz,  $\text{CDCl}_3$ ):  $\delta$  = 8.44 (s, 1 H), 7.72 (s, 1 H), 5.81 (br s, 1 H), 3.83 (s, 3 H), 3.23 (br s, 3 H);  $^{13}\text{C}$  NMR (101 MHz,  $\text{CDCl}_3$ ):  $\delta$  = 155.4, 153.1, 149.1, 139.9, 119.6, 29.6, 27.4; HRMS (ESI):  $m/z$ : calcd for  $[\text{C}_7\text{H}_{10}\text{N}_5]^+$ : 164.0936 found: 164.0931.

##### 4.5.2. 6-Chloro-*N*<sup>4</sup>-cyclopropylpyrimidine-4,5-diamine (intermediate I1 of compound 3)

To a stirred solution of 4,6-dichloropyrimidin-5-amine (1 g, 6.1 mmol) in isopropanol (12 mL), cyclopropylamine (2 equiv., 12.2 mmol, 849  $\mu\text{L}$ ) and  $\text{Et}_3\text{N}$  (2 equiv., 12.2 mmol, 1.7 mL) were added. The reaction mixture was stirred at 100 °C for 6 h in the microwave and concentrated under reduced pressure. The obtained residue was poured into water and the aqueous layer was extracted three times with EtOAc. The combined organic layers were washed with brine, dried over  $\text{MgSO}_4$ ,

filtered and concentrated under reduced pressure to afford the desired product as a brown solid (1.11 g, 98% yield).  $^1\text{H}$  NMR (400 MHz,  $\text{CDCl}_3$ ):  $\delta$  = 8.18 (s, 1 H), 5.14 (br s, 1 H), 3.38 (br s, 2 H), 2.92–2.82 (m, 1 H), 0.93–0.87 (m, 2 H), 0.62–0.56 (m, 2 H);  $^{13}\text{C}$  NMR (101 MHz,  $\text{CDCl}_3$ ):  $\delta$  = 156.0, 149.7, 143.0, 122.0, 24.2, 7.2 (s, 2 C).

##### 4.5.3. 6-Chloro-9-cyclopropyl-9H-purine (intermediate I2 of compound 3)

To a stirred solution of aniline intermediate I1 (1.1 g, 5.6 mmol) in triethylorthoformate (14 mL),  $\text{EtSO}_2\text{H}$  (12  $\mu\text{L}$ ) was added. The reaction mixture was stirred at 25 °C for 17 h and concentrated under reduced pressure. The crude residue was purified by column chromatography (EtOAc/heptane = 3:7 to 1:1 to 7:3) to afford the desired product as a white solid (78 mg, 84% yield).  $^1\text{H}$  NMR (400 MHz,  $\text{CDCl}_3$ ):  $\delta$  = 8.79 (s, 1 H), 8.13 (s, 1 H), 3.57–3.50 (m, 1 H), 1.32–1.16 (m, 4 H);  $^{13}\text{C}$  NMR (101 MHz,  $\text{CDCl}_3$ ):  $\delta$  = 152.8, 151.9, 150.8, 145.7, 131.7, 25.6, 5.9 (s, 2 C); LRMS (ESI):  $m/z$ : calcd for  $[\text{C}_8\text{H}_8\text{ClN}_4]^+$ : 195.0 found: 195.1.

##### 4.5.4. 9-Cyclopropyl-*N*-methyl-9H-purin-6-amine (compound 3)

To a stirred suspension of chloropurine intermediate I2 (100 mg, 0.51 mmol) in isopropanol (1.7 mL), methylamine (3 equiv., 1.54 mmol, 193  $\mu\text{L}$ , 8 M in EtOH) was added. The reaction mixture was stirred at 80 °C for 2.5 h in the microwave and concentrated under reduced pressure. The crude residue was purified by column chromatography (EtOAc/heptane = 1:1 to 7:3 to 10:0 to EtOAc/MeOH = 10:5 to 100:10) to afford the desired product as a white solid (98 mg, quantitative yield). HPLC Purity = 100%; Mp: 159–162 °C;  $^1\text{H}$  NMR (400 MHz,  $\text{CDCl}_3$ ):  $\delta$  = 8.47 (s, 1 H), 7.74 (s, 1 H), 5.70 (br s, 1 H), 3.43 (tt,  $J$  = 7.2, 3.6 Hz, 1 H), 3.22 (br s, 3 H), 1.24–1.16 (m, 2 H), 1.15–1.08 (m, 2 H);  $^{13}\text{C}$  NMR (101 MHz,  $\text{CDCl}_3$ ):  $\delta$  = 155.4, 153.2, 150.0, 139.9, 119.9, 27.4, 24.9, 5.7 (s, 2 C); HRMS (ESI)  $m/z$  calcd for  $[\text{C}_9\text{H}_{12}\text{N}_5]^+$ : 190.1093 found: 190.1087.

##### 4.5.5. *N*<sup>2</sup>,*N*<sup>6</sup>-Dimethyl-9H-purine-2,6-diamine (compound 4)

To a stirred suspension of 2,6-dichloro-9H-purine (100 mg, 0.49 mmol) in isopropanol (1.63 mL), methylamine (6 equiv., 2.96 mmol, 369  $\mu\text{L}$ , 8 M in EtOH) was added. The reaction mixture was stirred at 150 °C for 4 h in the microwave and concentrated under reduced pressure. The crude residue was purified by column chromatography (DCM/MeOH = 100:2 to 100:4 to 100:10) to afford the desired product as a white solid (27 mg, 28% yield). HPLC Purity = 100%; Mp: decomposed;  $^1\text{H}$  NMR (400 MHz,  $\text{MeOD}-d_4$ ):  $\delta$  = 7.65 (s, 1 H), 3.06 (s, 3 H), 2.92 (s, 3 H);  $^{13}\text{C}$  NMR (101 MHz,  $\text{DMSO}-d_6$ ):  $\delta$  = 160.6, 155.5, 152.0 (br s, 1 C), 135.3, 113.6 (br s, 1 C), 28.8, 27.3 (br s, 1 C); HRMS (ESI):  $m/z$ : calcd for  $[\text{C}_7\text{H}_{11}\text{N}_6]^+$ : 179.1045 found: 179.1040.

##### 4.5.6. *N*<sup>2</sup>,*N*<sup>6</sup>,9-Trimethyl-9H-purine-2,6-diamine (compound 5)

To a stirred suspension of 2,6-dichloro-9-methyl-9H-purine (200 mg, 0.99 mmol) in isopropanol (3 mL), methylamine (5 equiv., 4.93 mmol, 616  $\mu\text{L}$ , 8 M in EtOH) was added. The reaction mixture was stirred at 150 °C for 8 h in the microwave and concentrated under reduced pressure. The crude residue was purified by column chromatography (DCM/MeOH = 100:0 to 100:1 to 100:2 to 100:3 to 100:4 to 100:6) and the impure product was triturated in diethyl ether with a few drops of acetone, filtered and washed with diethyl ether to afford the desired product as a white solid (115 mg, 61% yield). HPLC Purity = 100%; Mp: 228–229 °C;  $^1\text{H}$  NMR (400 MHz,  $\text{MeOD}-d_4$ ):  $\delta$  = 7.62 (s, 1 H), 3.67 (s, 3 H), 3.05 (s, 3 H), 2.95 (s, 3 H);  $^{13}\text{C}$  NMR (101 MHz,  $\text{DMSO}-d_6$ ):  $\delta$  = 160.1, 155.1, 151.2, 137.4, 113.3, 28.8, 28.3, 26.8; HRMS (ESI):  $m/z$ : calcd for  $[\text{C}_8\text{H}_{12}\text{N}_6]^+$ : 193.1202 found: 193.1196.

#### Accession number

The atomic coordinates and structure factors for the 25 crystal

structures have been deposited in the Protein Data Bank (PDB) with the accession codes 7P88, 7P8A, 7P8B, 7P8F, 7PJP, 7PJ7, 7P87, 6YKZ, 6YKJ, 7PJQ, 6YNP, 7PJ8, 7PJ9, 6YKI, 6YNI, 6YL8, 6YKE, 6YNJ, 6YNL, 6YL9, 6YNM, 7PJB, 6YNK, 6YOQ, and 7PJA.

### Declaration of competing interest

The authors declare that they have no known competing financial interests or personal relationships that could have appeared to influence the work reported in this paper.

### Acknowledgements

We thank Beat Blattmann at the Protein Crystallization Center (University of Zurich) for assistance with crystallization screening. We thank Dr. Lars Wiedmer for help with some of the biochemical assays. The use of beamlines and user support at Swiss Light Source are gratefully acknowledged. We thank the Swiss National Supercomputing Center (CSCS) in Lugano and the Swedish National Infrastructure for Computing (SNIC) at the High-Performance Computing Center North (HPC2N), partially funded by the Swedish Research Council through grant agreement no. 2018–05973, for providing the computational resources. This work was supported by the International Postdoc Grant funded by the Swedish Research Council (Grant VR 2019-00608 to Y.L.) and an Excellence grant of the Swiss National Science Foundation (310030B\_189363 to A.C.).

### Appendix A. Supplementary data

Supplementary data to this article can be found online at <https://doi.org/10.1016/j.ejmc.2022.100057>.

### References

- C. He, Grand challenge commentary: RNA epigenetics? *Nat. Chem. Biol.* 6 (12) (2010) 863–865.
- K.D. Meyer, Y. Saletore, P. Zumbo, O. Elemento, C.E. Mason, S.R. Jaffrey, Comprehensive analysis of mRNA methylation reveals enrichment in 3' UTRs and near stop codons, *Cell* 149 (7) (2012) 1635–1646.
- J. Widagdo, V. Anggono, The m6A-epitranscriptomic signature in neurobiology: from neurodevelopment to brain plasticity, *J. Neurochem.* 147 (2) (2018) 137–152.
- J. Liu, X.Y. Do, C.Y. Chen, C. Chen, C. Liu, M.M. Xu, S.Q. Zhao, B. Shen, Y.W. Gao, D.L. Han, C. Hei, N<sup>6</sup>-methyladenosine of chromosome-associated regulatory RNA regulates chromatin state and transcription, *Science* 367 (6477) (2020) 580–586.
- J. Zhou, J. Wan, X.W. Gao, X.Q. Zhang, S.R. Jaffrey, S.B. Qian, Dynamic m<sup>6</sup>A mRNA methylation directs translational control of heat shock response, *Nature* 526 (7574) (2015) 591–594.
- R. Winkler, E. Gillis, L. Lasman, M. Safra, S. Geula, C. Soyris, A. Nachshon, J. Tai-Schmiedel, N. Friedman, T.K.L.T. Vu, M. Trilling, M. Mandelboim, J.H. Hanna, S. Schwartz, N. Stern-Ginossar, m<sup>6</sup>A modification controls the innate immune response to infection by targeting type I interferons, *Nat. Immunol.* 20 (2) (2019) 173–182.
- K. Tsai, H.P. Bogerd, E.M. Kennedy, A. Emery, R. Swanstrom, B.R. Cullen, Epitranscriptomic addition of m<sup>6</sup>A regulates HIV-1 RNA stability and alternative splicing, *Genes Dev.* 35 (13–14) (2021) 992–1004.
- S.Y. Wang, P.W. Chai, R.B. Jia, R.B. Jia, Novel insights on m<sup>6</sup>A RNA methylation in tumorigenesis: a double-edged sword, *Mol. Cancer* 17 (101) (2018), <https://doi.org/10.1186/s12943-018-0847-4>.
- I.A. Roundtree, M.E. Evans, T. Pan, C. He, Dynamic RNA modifications in gene expression regulation, *Cell* 169 (7) (2017) 1187–1200.
- K.D. Meyer, S.R. Jaffrey, Rethinking m<sup>6</sup>A readers, writers, and erasers, *Annu. Rev. Cell Dev. Biol.* 33 (2017) 319–342.
- Y. Wang, Y. Li, J.I. Toth, M.D. Petroski, Z.L. Zhang, J.C. Zhao, N<sup>6</sup>-methyladenosine modification destabilizes developmental regulators in embryonic stem cells, *Nat. Cell Biol.* 16 (2) (2014) 191–198.
- J.Z. Liu, Y.N. Yue, D.L. Han, X. Wang, Y. Fu, L. Zhang, G.F. Jia, M. Yu, Z.K. Lu, X. Deng, Q. Dai, W.Z. Chen, C. He, A METTL3-METTL14 complex mediates mammalian nuclear RNA N<sup>6</sup>-adenosine methylation, *Nat. Chem. Biol.* 10 (2) (2014) 93–95.
- G.F. Jia, Y. Fu, X. Zhao, Q. Dai, G.Q. Zheng, Y. Yang, C.Q. Yi, T. Lindahl, T. Pan, Y.G. Yang, C. He, N<sup>6</sup>-Methyladenosine in nuclear RNA is a major substrate of the obesity-associated FTO, *Nat. Chem. Biol.* 7 (12) (2011) 885–887.
- G.Q. Zheng, J.A. Dahl, Y.M. Niu, P. Fedorcsak, C.M. Huang, C.J. Li, C.B. Vagbo, Y. Shi, W.L. Wang, S.H. Song, Z.K. Lu, R.P.G. Bosmans, Q. Dai, Y.J. Hao, X. Yang, W.M. Zhao, W.M. Tong, X.J. Wang, F. Bogdan, K. Furu, Y. Fu, G.F. Jia, X. Zhao, J. Liu, H.E. Krokan, A. Klungland, Y.G. Yang, C. He, ALKBH5 is a mammalian RNA demethylase that impacts RNA metabolism and mouse fertility, *Mol. Cell* 49 (1) (2013) 18–29.
- D. Dominissini, S. Moshitch-Moshkovitz, S. Schwartz, M. Salmon-Divon, L. Ungar, S. Osenberg, K. Cesarkas, J. Jacob-Hirsch, N. Amariglio, M. Kupiec, R. Sorek, G. Rechavi, Topology of the human and mouse m<sup>6</sup>A RNA methylomes revealed by m<sup>6</sup>A-seq, *Nature* 485 (7397) (2012) 201–206.
- P.J. Hsu, Y.F. Zhu, H.H. Ma, Y.H. Guo, X.D. Shi, Y.Y. Liu, M.J. Qi, Z.K. Lu, H.L. Shi, J.Y. Wang, Y.W. Cheng, G.Z. Luo, Q. Dai, M.X. Liu, X.J. Guo, J.H. Sha, B. Shen, C. He, Ythdc2 is an N<sup>6</sup>-methyladenosine binding protein that regulates mammalian spermatogenesis, *Cell Res.* 27 (9) (2017) 1115–1127.
- X. Wang, Z.K. Lu, A. Gomez, G.C. Hon, Y.N. Yue, D.L. Han, Y. Fu, M. Parisien, Q. Dai, G.F. Jia, B. Ren, T. Pan, C. He, N<sup>6</sup>-methyladenosine-dependent regulation of messenger RNA stability, *Nature* 505 (7481) (2014) 117–120.
- Y.C. Zhao, Y.F. Shi, H.F. Shen, W.Z. Xie, m<sup>6</sup>A-binding proteins: the emerging crucial performers in epigenetics, *J. Hematol. Oncol.* 13 (1) (2020).
- W. Xiao, S. Adhikari, U. Dahal, Y.S. Chen, Y.J. Hao, B.F. Sun, H.Y. Sun, A. Li, X.L. Ping, W.Y. Lai, X. Wang, H.L. Ma, C.M. Huang, Y. Yang, N. Huang, G.B. Jiang, H.L. Wang, Q. Zhou, X.J. Wang, Y.L. Zhao, Y.G. Yang, Nuclear m<sup>6</sup>A reader YTHDC1 regulates mRNA splicing, *Mol. Cell* 61 (4) (2016) 507–519.
- I.A. Roundtree, G.Z. Luo, Z.J. Zhang, X. Wang, T. Zhou, Y.Q. Cui, J.H. Sha, X.X. Huang, L. Guerrero, P. Xie, E. He, B. Shen, C. He, YTHDC1 mediates nuclear export of N<sup>6</sup>-methyladenosine methylated mRNAs, *Elife* 6 (2017) e31311.
- D.P. Patil, C.K. Chen, B.F. Pickering, A. Chow, C. Jackson, M. Guttman, S.R. Jaffrey, m<sup>6</sup>A RNA methylation promotes XIST-mediated transcriptional repression, *Nature* 537 (7620) (2016) 369–373.
- W. Xu, J. Li, C. He, J. Wen, H. Ma, B. Rong, J. Diao, L. Wang, J. Wang, F. Wu, L. Tan, Y.G. Shi, Y. Shi, H. Shen, METTL3 regulates heterochromatin in mouse embryonic stem cells, *Nature* 591 (7849) (2021) 317–321.
- J. Liu, M. Gao, J. He, K. Wu, S. Lin, L. Jin, Y. Chen, H. Liu, J. Shi, X. Wang, L. Chang, Y. Lin, Y.L. Zhao, X. Zhang, M. Zhang, G.Z. Luo, G. Wu, D. Pei, J. Wang, X. Bao, J. Chen, The RNA m<sup>6</sup>A reader YTHDC1 silences retrotransposons and guards ES cell identity, *Nature* 591 (7849) (2021) 322–326.
- H. Shima, M. Matsumoto, Y. Ishigami, M. Ebina, A. Muto, Y. Sato, S. Kumagai, K. Ochiai, T. Suzuki, K. Igarashi, S-adenosylmethionine synthesis is regulated by selective N<sup>6</sup>-adenosine methylation and mRNA degradation involving METTL16 and YTHDC1, *Cell Rep.* 21 (12) (2017) 3354–3363.
- Y. Cheng, W. Xie, B.F. Pickering, K.L. Chu, A.M. Savino, X. Yang, H. Luo, D.T. Nguyen, S. Mo, E. Barin, A. Velleca, T.M. Rohwetter, D.J. Patel, S.R. Jaffrey, M.G. Kharas, N<sup>6</sup>-Methyladenosine on mRNA facilitates a phase-separated nuclear body that suppresses myeloid leukemic differentiation, *Cancer Cell* 39 (7) (2021) 958–972, e8.
- R. Shi, S. Ying, Y. Li, L. Zhu, X. Wang, H. Jin, Linking the YTH domain to cancer: the importance of YTH family proteins in epigenetics, *Cell Death Dis.* 12 (4) (2021) 346.
- C. Xu, X. Wang, K. Liu, I.A. Roundtree, W. Tempel, Y. Li, Z. Lu, C. He, J. Min, Structural basis for selective binding of m<sup>6</sup>A RNA by the YTHDC1 YTH domain, *Nat. Chem. Biol.* 10 (11) (2014) 927–929.
- Y. Li, R.K. Bedi, L. Wiedmer, X. Sun, D. Huang, A. Caflich, Atomistic and thermodynamic analysis of N<sup>6</sup>-methyladenosine (m<sup>6</sup>A) recognition by the reader domain of YTHDC1, *J. Chem. Theor. Comput.* 17 (2) (2021) 1240–1249.
- M. Krepl, F.F. Damberger, C. von Schroetter, D. Theler, P. Pokorna, F.H. Allain, J. Sponer, Recognition of N<sup>6</sup>-methyladenosine by the YTHDC1 YTH domain studied by molecular dynamics and NMR spectroscopy: the role of hydration, *J. Phys. Chem. B* 125 (28) (2021) 7691–7705.
- Y.Z. Li, R.K. Bedi, L. Wiedmer, D.Z. Huang, P. Sledz, A. Caflich, Flexible binding of m<sup>6</sup>A reader protein YTHDC1 to its preferred RNA motif, *J. Chem. Theor. Comput.* 15 (12) (2019) 7004–7014.
- R.K. Bedi, D. Huang, L. Wiedmer, Y. Li, A. Dolbois, J.A. Wojdyla, M.E. Sharpe, A. Caflich, P. Sledz, Selectively disrupting m<sup>6</sup>A-dependent protein-RNA interactions with fragments, *ACS Chem. Biol.* 15 (3) (2020) 618–625.
- The PyMOL Molecular Graphics System, Version 2.2, Schrödinger, LLC.
- L. Wiedmer, S.A. Eberle, R.K. Bedi, P. Sledz, A. Caflich, A reader-based assay for m<sup>6</sup>A writers and erasers, *Anal. Chem.* 91 (4) (2019) 3078–3084.
- MarvinSketch 21.20.0, ChemAxon. <http://www.chemaxon.com>.
- S. Wlodek, A.G. Skillman, A. Nicholls, Ligand entropy in gas-phase, upon solvation and protein complexation. Fast estimation with quasi-Newton hessian, *J. Chem. Theor. Comput.* 6 (7) (2010) 2140–2152.
- SZYBKI 2.4.0.0, OpenEye Scientific Software, S. F., NM, <http://www.eyesopen.com>.
- O. Trott, A.J. Olson, Software news and update AutoDock Vina: improving the speed and accuracy of docking with a new scoring function, efficient optimization, and multithreading, *J. Comput. Chem.* 31 (2) (2010) 455–461.
- K. Goossens, B. Wroblowski, C. Langini, H. van Vlijmen, A. Caflich, H. De Winter, Assessment of the fragment docking program SEED, *J. Chem. Inf. Model.* 60 (10) (2020) 4881–4893.
- N. Majeux, M. Scarsi, J. Apostolakis, C. Ehrhardt, A. Caflich, Exhaustive docking of molecular fragments with electrostatic solvation, Proteins-Structure Function and Bioinformatics 37 (1) (1999) 88–105.
- X.Y. Chen, H.C. Liu, W.C. Xie, Y. Yang, Y.C. Wang, Y.R. Fan, Y. Hua, L. Zhu, J.N. Zhao, T. Lu, Y.D. Chen, Y.M. Zhang, Investigation of crystal structures in structure-based virtual screening for protein kinase inhibitors, *J. Chem. Inf. Model.* 59 (12) (2019) 5244–5262.
- T. Sterling, J.J. Irwin, ZINC 15–ligand discovery for everyone, *J. Chem. Inf. Model.* 55 (11) (2015) 2324–2337.
- M. Scarsi, J. Apostolakis, A. Caflich, Comparison of a GB solvation model with explicit solvent simulations: potentials of mean force and conformational preferences of alanine dipeptide and 1,2-dichloroethane, *J. Phys. Chem. B* 102 (18) (1998) 3637–3641.

- [43] M. Scarsi, J. Apostolakis, A. Caflisch, Continuum electrostatic energies of macromolecules in aqueous solutions, *J. Phys. Chem.* 101 (43) (1997) 8098–8106.
- [44] Y. Xu, K. Vanommeslaeghe, A. Aleksandrov, A.D. MacKerell, L. Nilsson, Additive CHARMM force field for naturally occurring modified ribonucleotides, *J. Comput. Chem.* 37 (10) (2016) 896–912.
- [45] J. Huang, A.D. MacKerell, CHARMM36 all-atom additive protein force field: validation based on comparison to NMR data, *J. Comput. Chem.* 34 (25) (2013) 2135–2145.
- [46] Maestro 11.5, S., LLC, New York, NY, 2018.
- [47] G.J. Martyna, M.L. Klein, M. Tuckerman, Nose-hoover chains - the canonical ensemble via continuous dynamics, *J. Chem. Phys.* 97 (4) (1992) 2635–2643.
- [48] S.E. Feller, Y.H. Zhang, R.W. Pastor, B.R. Brooks, Constant-pressure molecular-dynamics simulation - the Langevin piston method, *J. Chem. Phys.* 103 (11) (1995) 4613–4621.
- [49] K. Vanommeslaeghe, E. Hatcher, C. Acharya, S. Kundu, S. Zhong, J. Shim, E. Darian, O. Guvench, P. Lopes, I. Vorobyov, A.D. Mackerell Jr., CHARMM general force field: a force field for drug-like molecules compatible with the CHARMM all-atom additive biological force fields, *J. Comput. Chem.* 31 (4) (2010) 671–690.
- [50] U. Essmann, L. Perera, M.L. Berkowitz, T. Darden, H. Lee, L.G. Pedersen, A smooth particle mesh Ewald method, *J. Chem. Phys.* 103 (19) (1995) 8577–8593.
- [51] B.R. Brooks, C.L. Brooks, A.D. Mackerell, L. Nilsson, R.J. Petrella, B. Roux, Y. Won, G. Archontis, C. Bartels, S. Boresch, A. Caflisch, L. Caves, Q. Cui, A.R. Dinner, M. Feig, S. Fischer, J. Gao, M. Hodoscek, W. Im, K. Kuczera, T. Lazaridis, J. Ma, V. Ovchinnikov, E. Paci, R.W. Pastor, C.B. Post, J.Z. Pu, M. Schaefer, B. Tidor, R.M. Venable, H.L. Woodcock, X. Wu, W. Yang, D.M. York, M. Karplus, CHARMM: the biomolecular simulation program, *J. Comput. Chem.* 30 (10) (2009) 1545–1614.